Research Article | Vol. 30, No. 23 / 7 Nov 2022 / Optics Express 42015
Optics EXPRESS

High-sensitivity operation of an unshielded single cell radio-frequency atomic magnetometer

HAN YAO, BENJAMIN MADDOX, AND F. RENZONI*

Department of Physics and Astronomy, University College London, Gower Street, London WC1E 6BT, UK
**f.renzoni@ucl.ac.uk*

Abstract: Real-world applications of atomic magnetometers require the ability to operate them with high-sensitivity in the presence of magnetic noise. In the present work, high-sensitivity operation of unshielded atomic magnetometers in a magnetically noisy environment is demonstrated. The distinguishing feature of the demonstrated approach is the implementation of active in-situ bias field stabilization using multiple fluxgate magnetometers. This is combined with the use of a counter-propagating pump and triple-pass probe configuration, to maximize the atomic polarization and the probe rotation respectively, so to reach high-sensitivity. The improvement in sensitivity of the unshielded system with respect to previous realizations is fully characterized, with the contributions of the different modifications of the apparatus individually quantified. The presented set-up is suitable for the detection of long-range magnetic fields, where shielding or differential measurements using multi-sensor set-ups do not constitute viable options.

1. Introduction

Atomic magnetometers [1] have attracted growing interest due to their demonstrated extreme sensitivity. Sub-fT/Hz$^{1/2}$ sensitivity in magnetically shielded environment was demonstrated [2,3], thus rivalling the best SQUID magnetometers. This has opened the path to a wealth of applications for shielded atomic magnetometers, from magneto-cardiography (MCG) [4,5] and magneto-encephalography (MEG) [6] to low-field nuclear magnetic resonance (NMR) [7] and nuclear quadrupole resonance (NQR) detection [8].

The performances of atomic magnetometers are significantly affected by ambient magnetic noise. Ambient noise within a certain frequency range may degrade, via nonlinear effects, measurements of a magnetic field in a different frequency range. This limitation is usually overcome by operating the atomic magnetometer in a magnetically shielded environment or, in case of spatially rapidly decaying field, by the use of differential measurements with a multiple sensor set-up [2,3,9–17]. Here we focus on scenarios, such as active underwater detection via electromagnetic induction, where shielding is impossible and the long-range nature of the considered magnetic fields makes the use of differential measurements unsuitable. We specifically consider radio-frequency atomic magnetometers (RF-AMs) [18], as those used in active underwater detection [19] and electromagnetic induction imaging [20,21], for which low-frequency ambient noise degrades the quality of the measurement at higher frequency via the bias field couplings. We demonstrate that high-sensitivity unshielded operation in the presence of ambient noise can be reached by the combination of three factors: in-situ active stabilization of the bias field, counter-propagating pumping and triple-pass probing. Detailed experimental analysis is carried out for the specific case of a ^{87}Rb radio-frequency magnetometer, and the contributions of the three different factors leading to improvement in sensitivity are individually quantified.

#476016 https://doi.org/10.1364/OE.476016
Journal © 2022 Received 19 Sep 2022; revised 17 Oct 2022; accepted 21 Oct 2022; published 31 Oct 2022

Optics EXPRESS

2. RF-AM set-up: general features

This Section introduces the features of the RF-AM common to all the configurations examined in this work. The core of the atomic magnetometer used in this work is a $25 \times 25 \times 25$ mm^3 quartz vapor cell filled with isotopically enriched ^{87}Rb and 40 Torr of N_2 as buffer and quenching gas. The cell can be heated so to reach a high atomic density, with the help of six heating pads. These are high-Tg printed circuit boards (PCBs) of copper traces wired in pairs. The pads are driven with alternating currents at 51 kHz supplied by a full bridge circuit. The cell, the heating pads and a temperature sensor are enclosed in a 3D-printed high temperature plastic enclosure. The heater is turned off during the measurements so to prevent generation of additional magnetic field noise and spurious DC magnetic fields.

Figure 1 illustrates the basic structure of the RF-AM considered in this work. The atomic sample is polarized by the application of a pair of circularly polarized counter-propagating pump beams along the z-axis in the presence of a collinear bias magnetic field. The atomic precession is driven by an RF field provided by a pair of Helmholtz coils symmetrically located with respect to the cell and having their axis aligned to the y axis. The Helmholtz coil pair is driven by the reference signal of a lock-in amplifier (LIA, Zurich Instruments HF2LI). The spin precession is readout by a linearly polarized probe beam along x axis, whose rotation is monitored by a balanced polarimeter and demodulated by the LIA. We notice here that the angle of polarization rotation is given by

$$\phi = \frac{1}{2}\arcsin\left(\frac{I_1 - I_2}{I_1 + I_2}\right) \simeq \frac{1}{2}\left(\frac{I_1 - I_2}{I_1 + I_2}\right), \tag{1}$$

where I_1 and I_2 indicate the intensities of the orthogonal components of the linear polarized beam measured by the two channels of the polarimeter. In our single-pumping-single-probe set up, the optical rotation angle was measured to be 1.23 mrad at 85 °C. The measured small rotations $\phi \ll 1$ validate the use of the approximation in Eq. (1). However, throughout the manuscript, unless explicitly stated, measurements of $I_1 - I_2$ are presented, as directly readout by the polarimeter. This is because the value of the SNR and thus the sensitivity are directly generated from this quantity, and a normalization by $I_1 + I_2$ would not affect these quantities. The magnetic field and the pump-probe beams arrangements are described in detail in the following.

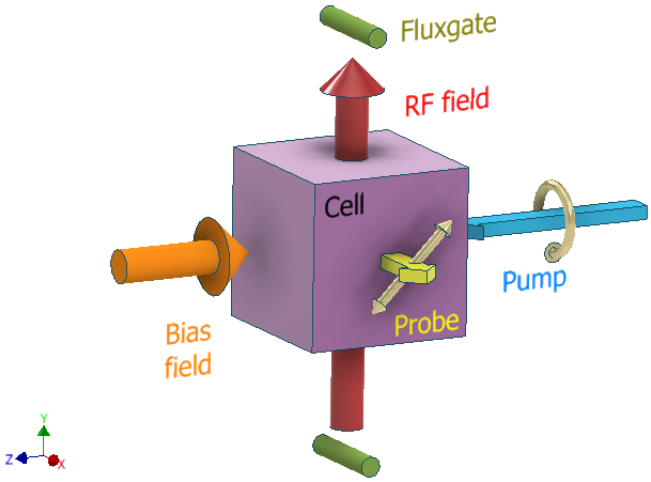

Fig. 1. Illustration of the RF-AM (not to scale) indicating the directions of the laser beams and magnetic fields, and the positions of the fluxgate sensors. The golden arrows show the polarization of light.

Optics EXPRESS

Throughout the manuscript we will characterize the system by providing the standard figures of AC sensitivity at a given representative frequency as well as the DC sensitivity.

The DC sensitivity refers to the smallest detectable shift of the bias field and is given by

$$\delta B_{DC} = \frac{\hbar}{g_F \mu_B} \frac{\Gamma}{\sqrt{RBW}\,\mathrm{SNR}}, \tag{2}$$

where μ_B is the Bohr magneton, g_F is the Landé factor, $\hbar$ is Planck's constant, RBW is the resolution bandwidth and Γ is the full width at half maximum (FWHM) of the magnetic resonance. The SNR is measured as the square root of the ratio between the maximum value of the power spectrum density (PSD) with the RF field on and the mean value of the noise power spectrum density with the RF field turned off, which is also referred to as the noise floor. The AC sensitivity (δB_{AC}) is defined as

$$\delta B_{\mathrm{AC}} = \frac{B_{RF}}{\mathrm{SNR}\sqrt{RBW}}. \tag{3}$$

where B_{RF} is the RF field applied for calibration purposes.

We notice that the DC sensitivity is purely reported to be consistent with standard characterization of magnetometers, and does not imply that the proposed system is to be used for DC field measurements. This is because the stabilization of the bias field used in this work leads to an automatic compensation of any additional static field, as specified in the following.

3. Active in-situ stabilization of the bias field

Active stabilization of the bias field has proven to be essential in previous experimental work with unshielded RF-AMs [20,22]. In all these experimental realizations, the error signal for the active stabilization was generated with the help of a fluxgate magnetometer placed in close proximity of the atomic vapor. While this approach significantly increased the stability of the sensor and improved its sensitivity, residual detrimental effects of the low-frequency ambient magnetic field remained as the displacement between the atomic vapor and the fluxgate magnetometer does not allow for an optimal magnetic field compensation in presence of inhomogeneity of the ambient field. The issue of stabilising the magnetic field at a given location with no access to it can be addressed by using multiple sensors, as shown in previous work with sets of magneto-resistive probes [23] and Hall sensors [24] placed outside the exclusion volume defined by the requirements of the experiment. In the present work, an effectively in-situ cancellation of the magnetic field is performed by using two fluxgate magnetometers, symmetrically displaced with respect to the atomic vapor cell. By taking the average of the two values of the magnetic field measured by the two sensors, a very good approximation of the magnetic field at the centre of the cell can be derived, and used for the stabilization circuit. This proved to successfully improve the sensitivity of the atomic magnetometer. The use of two fluxgate magnetometers also allows for an increased distance from the atomic magnetometer, reducing the detrimental effect of the residual field generated by the fluxgate magnetometer on the sensor.

In detail, two triaxial fluxgate magnetometers (Stefan-Meyer FLC3-70) were placed symmetrically with respect to the vapor cell, along a line orthogonal to the bias field direction, as shown in Fig. 1. The distance of each fluxgate from the cell centre was 97.5 mm. Only one axis of the fluxgate was used for the active stabilization, and precisely the axis in the direction of the bias field. The two outputs of the fluxgate magnetometers were added and used as an input for the proportional-integral-derivative (PID) controller part of the feedback circuit. The bandwidth of the feedback loop is determined by the bandwidth of the fluxgate, which is 1 kHz. Thus, the magnetometer is suited to measure AC fields above 1 kHz, as below this frequency the compensation system will act to attenuate the magnetic field. We note that with respect to

Optics EXPRESS

previous work [20,22] where triaxial active compensation was used, we found here that active stabilization along the bias field direction is sufficient for high-sensitivity operation, thus only the field in that direction is actively stabilized in the set-up described in this work. AC sensitivity is reported at the frequency of 418 kHz, which was chosen as representative of a noisy band of the ambient electromagnetic spectrum, and also to allow comparison with previous work [25] where bias field stabilization was implemented using a single fluxgate magnetometer (Bartington MAG690-1000) placed along the bias direction next to the oven on the path of the pumping beam leaving the cell.

Table 1 and Fig. 2 show respectively the sensitivities and the noise spectra for the two configurations. As shown in Fig. 2, the SNR is measured as the square root of the ratio between the peak value of the power spectrum density with the RF field turned on and the mean value of the noise power spectrum density within the range of linewidth when the RF field is turned off. The measurements were taken under the same conditions, while the PID settings were adjusted to maximize the SNR separately. The configuration with two fluxgate magnetometers generates a less noisy spectrum and a narrower magnetic resonance.

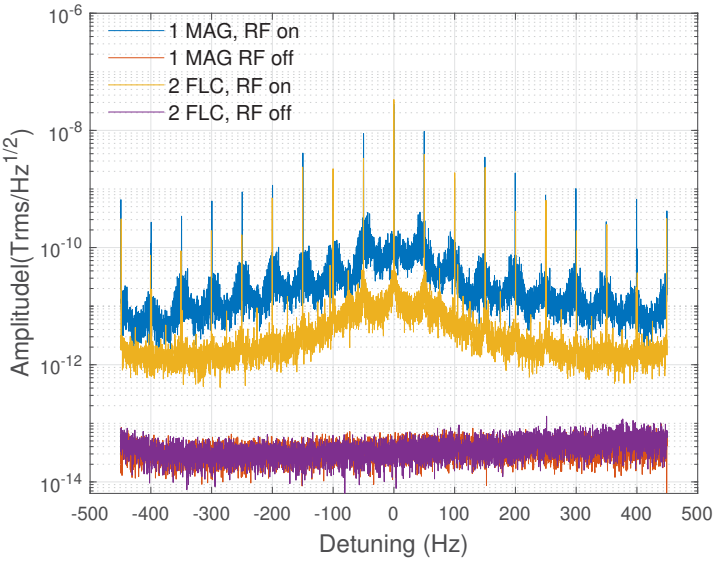

Fig. 2. Comparison of noise spectra taken in different configurations of bias field stabilization. Both measurements were taken under the same conditions of an operating frequency of 418 kHz, a cell temperature of 108 °C, counter-propagating pumping with a total power of 22.4 mW, a single pass probe of 3.9 mW before the cell and a probe frequency detuning of about 4 GHz in the blue of the ^{87}Rb $F = 2 \rightarrow F' = 3$ D2 line transition. The spectra are calibrated by the same RF field, whose amplitude was determined by measuring the voltage across a non-inductive resistor connected in series to the RF coil driving the atomic precession.

Table 1. DC and AC sensitivity for different configurations of the bias field stabilization.

Fluxgate	HWHM (Hz)	SNR	δB_{DC} (fT/Hz$^{1/2}$)	δB_{AC} (fT/Hz$^{1/2}$)
One MAG690-1000	540	8.04E+05	30.6	41.8
Two FLC3-70	437	8.92E+05	22.3	37.7

Compensation of the ambient magnetic field in the two directions orthogonal to the bias field was performed by manually varying the current in two additional Helmholtz coils pairs so to minimize the magnetic resonance frequency. Three additional anti-Helmholtz coil pairs were

Optics EXPRESS

used to cancel magnetic field gradients. The optimal working point was found by monitoring the magnetic resonance, and minimising its linewidth while varying the currents in anti-Helmholtz coil pairs along each direction.

4. Counter-propagating pumping

Increasing the density of the atomic vapor is a common approach to increase the sensitivity of an atomic magnetometer. The fundamental sensitivity of an atomic magnetometer determined by spin-projection noise can be derived as [1]

$$\delta B_{SNL} = \frac{1}{\gamma\sqrt{ntVT_2}}, \tag{4}$$

where n is the density of alkali atoms, γ is their gyromagnetic ratio, T_2 is the transverse relaxation time, V is the cell volume and t is the measurement time. The above expression implies that by increasing the atomic number density in the vapor cell leads to an improvement of the fundamental sensitivity. However, the high number density of the optically pumped atomic vapor leads to strong absorption of the pump beam and generates a gradient of the electronic spin polarization of the atoms. This is a significant issue, as maintaining a large uniform atomic polarization at high atomic densities is essential for operating the atomic magnetometer at high sensitivity [26,27].

A homogenous spin polarization along the propagation of the pumping beam can be generated in a straightforward way by saturating the atomic vapor with excess pumping power. However this approach may induce relaxation. At a certain pumping level the light broadening Γ_{pump} exceeds the transit-time broadening Γ_{tr}

$$\frac{\Gamma_{pump}}{\Gamma_{tr}} = \frac{\Omega_R^2/\Gamma_0}{\Gamma_{tr}} > 1, \tag{5}$$

and one can observe a decreased sensitivity caused by the pumping effect [28]. Here Ω_R is the Rabi frequency and Γ_0 is the natural linewidth of the transition. As there exists an optimum value of polarization for high sensitivity instead of the saturated one [29,30], over pumping was not adopted here for a more uniform polarization. Several methods to produce uniform polarization have been reported, such as hybrid optical pumping via spin-exchange collisions of two different alkali metal species [31], and optimising the diameter and power of the pump beam with fine adjustment [26].

At 100 °C, the saturated density of the rubidium vapor is estimated to be $6.02 \times 10^{12}\text{cm}^{-3}$ [32] and the optical depth of our cell was measured to be 0.73. In this work the counter-propagating pumping method [8,33] was adopted to maintain a near-optimal pumping rate throughout the cell. The optical set-up for the counter-propagating pump beams configuration is shown in Fig. 3. The pumping beam was expanded to 10 mm in diameter while the probe was expanded to 7 mm in diameter. The cell was illuminated by two circularly polarized counter-propagating pumping beams simultaneously, aligned parallel/anti-parallel with the bias field direction. The ellipticity of the two counter-propagating beams was optimized by using the magnetic resonance. The bias frequency was increased to 3 MHz where obvious splitting can be observed due to second order Zeeman effect. Magnetic resonances were monitored when the cell was illuminated by each beam separately. Fine tuning of the ellipticity of the beams was carried out by ensuring that the magnetic resonances observed were identical for each single pump beam.

Figure 4 shows the linewidth and amplitude of the magnetic resonance with the bias magnetic field tuned to 418 kHz as a function of the pumping beam power under single and counter-propagating pumping separately. The light narrowing effect can be observed both for the single and counter-propagating pump beam configuration. The minimum linewidth is essentially the same for both configurations, and obtained for the same total power, while the signal amplitude

Optics EXPRESS

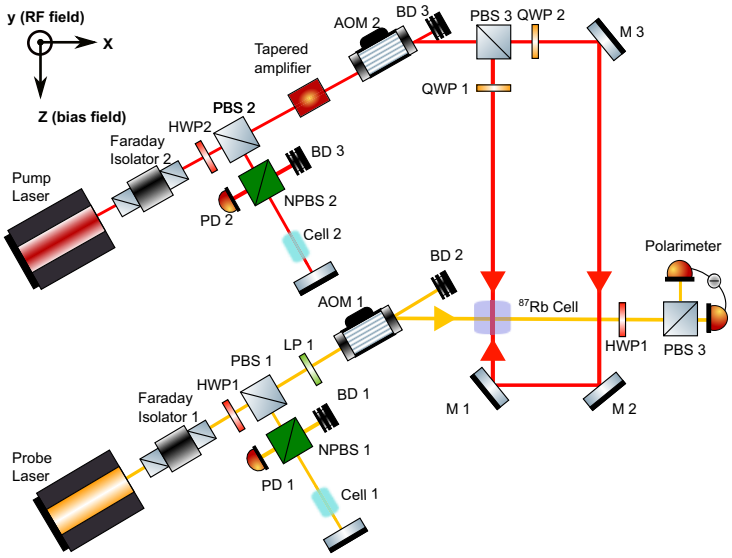

Fig. 3. Optical set-up for the counter-propagating pump beams configuration. AOM: acousto-optic modulator; HWP: half-wave plate; QWP: quarter-wave plate; LP: linear polarizer; BD: beam dump; M: mirror; PBS: polarising beam splitter; NPBS: non-polarising beam splitter.

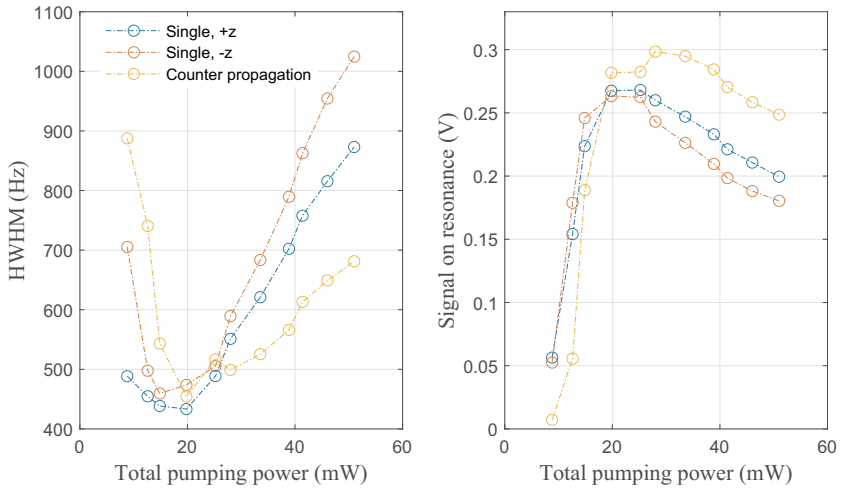

Fig. 4. Linewidth and amplitude of the magnetic resonance vs pump power. For a given AOM level, the total power of the single pump and two-arm counter-propagating pump is the same, i.e. for the single pump the entire power is sent in the single beam, while for the counter-propagating pump configuration the power is split evenly between the two beams. Data are for a cell temperature of 108 °C, a blue probe frequency detuning of 4 GHz and a probe power of 4 mW.

Optics EXPRESS

is larger for the counter-propagating pumping configuration. This indicates a more uniform larger polarization in the counter-propagating pumping case. For the counter-propagating pump configuration the detuning of the probe beam was optimized, with a value of about 4 GHz in the blue of the ^{87}Rb D2 line $F = 2 \rightarrow F' = 3$ resonance found to provide the best sensitivity.

5. Multi-pass probe

To further improve the signal strength of the magnetometer, double-, triple- and four-pass probe configurations were considered and characterized. In multi-pass configurations the probe polarization rotation is enhanced by a factor equal to the number of passes, as we verified experimentally for all considered cases.

The different optical set-ups for these configurations are shown in Fig. 5. A second pass of the probe beam was introduced by retro-reflecting the beam, with the read-out of the beam obtained by introducing a NPBS before the vapor cell. For this configuration the maximum attainable probe beam power decreased from 6 mW to 3 mW. The third and fourth passes were then generated by additional retro-reflection at a small angles with the first two passes.

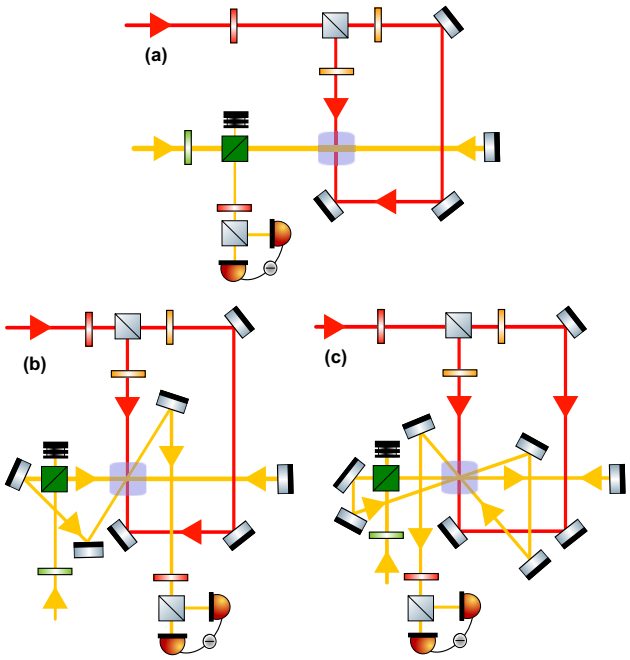

Fig. 5. Optical set-ups for the double- (a), triple- (b) and four-pass (c) probe configuration considered in this work. Distances and angles are exaggerated for easier reading. Symbols are the same as those in Fig. 3.

Unlike the 42-pass Herriot-type multipass rubidium cell reported in [34] that increased the path length of the probe beam by two orders of magnitude, in this work the multipass probing did not involve mirrors internal to the vapor cell. Despite the significantly smaller number of passes, the present configuration still leads to an enhancement of the SNR and is of simple realization. Additionally, the present configuration does not require to reduce the beam diameter. Thus a beam filling the entire cell window aperture, of 7 mm diameter, with little beam clipping at the entrance and exit of the cell could be used, without any reduction in interaction volume with respect to the single-beam configuration.

Optics EXPRESS

Table 2. DC (δB_{DC}) and AC (δB_{AC}) sensitivities for single-, double-, triple-, and four-pass probe configurations.[a]

No.	Probe pass	P_{probe} (mW)	P_{pump} (mW)	D_{probe} (mm)	D_{pump} (mm)	T (°C)	T_{NDF}	HWHM (Hz)	SNR	δB_{DC} (fT/Hz$^{1/2}$)	δB_{AC} (fT/Hz$^{1/2}$)
1	single	6	19.8	7	7	108	1.30%	320	5.01E+05	29.1	67.1
2		**3**	19.8	7	10	108	1.30%	312	3.34E+05	42.6	101
3	double	3	19.8	7	10	108	1.30%	309	1.83E+05	76.7	183
4		3	19.8	7	10	108	**16%**	319	9.27E+05	15.7	36.3
5		3	17.2	7	10	108	**30%**	318	1.00E+06	14.4	33.5
6	triple	3	22.4	7	10	108	100%	268	1.12E+06	10.8	29.9
7		3	28	12.5	**13**	107	100%	234	1.29E+06	8.28	26.1
8	four	3	35.2	12.5	13	107	100%	288	9.15E+05	14.3	36.7

[a]These represent all accessible multi-pass probe configurations given the available probe power. Probe pass represents the number times that the probe beam traverses the cell. P_{probe} and P_{pump} represent probe and pump power measured before cell, D_{probe} and D_{pump} represent diameters of the probe and pump beam, T_{NDF} represents the transmission of ND filters positioned before the polarimeter, T represents the cell temperature. All data are for a frequency of 418 kHz, a sinusoidal RF field of magnitude of 47.5 nT_{rms}, and uniformity better than 0.05% over the dimension of the vapor cell. For each considered number of passes, the control parameter whose value was varied in a given line with respect to the previous one is highlighted in bold. A given variation of a control parameter may require re-optimization of other parameters.

Row 1 to 5 in Table 2 compares the performances of the magnetometer under single and double pass probe using counter-propagating pumping beams. The SNR and the DC and AC sensitivities were determined and reported in this table. To avoid the saturation of the differential photo detector (PDB210A/M, Thorlabs) and the LIA, and absorptive neutral density filters of different transmissions (Transmissions at 780 nm: NENIR20A, 30%; NE10A, 16%; NE30A, 1.3%, Thorlabs) were added on the polarimeter and listed in the tables.

The probe power was optimized after adding the NPBS. The highest signal to noise ratio was obtained at the current maximum of 3 mW, with 17.2 mW total power of counter-propagating pumping, probe detuning of 4 GHz from the ^{87}Rb $F = 2 \rightarrow F' = 3$ D2 line transition, cell temperature of 108 °C and 20 dB attenuation on the polarimeter signal. The following tests for double pass probe were all carried out at this probe power. First, the probe power was decreased for the single-pass probe configuration to determine the role of the probe power in the magnetometer performances. Results reported in rows 1 and 2 of Table 2 show that a decrease in probe power is detrimental to the magnetometer performances. This should be taken into account when introducing a second probe pass as the resulting probe power reduction may limit the increase in SNR expected from the increase in number of passes. The simple addition of a second pass does not lead to an improvement in performances, in agreement with the above findings. Indeed, comparing rows 2 and 3 of Table 2, we find that the simple introduction of a double pass decreased the signal strength while the noise level was unchanged, at variance with the expected effect of a double pass probe. However, this is due to a decrease in probe power following the double pass transmission through the cell, and by replacing the ND filter in front of the polarimeter with one with less absorption, the double pass configuration led to the expected increase in SNR, as shown in rows 3, 4 and 5 of Table 2.

Additional experiments were performed for a triple-pass probe configuration. A third pass of the probe beam was added after the double pass and was sent through the cell at a small angle. This also circumvented the problem of saturation of the polarimeter and avoided using ND filters. In fact, we verified that the raw polarimeter signal was brought away from saturation due to the third pass through the vapor cell. The third pass configuration improved further the magnetometer performances. As shown in row 5 and 6 of Table 2, the sensitivities were further improved compared with double pass probe at the same conditions of 108 °C, 3 mW probe power and 20 dB signal attenuation.

Optics EXPRESS

Additional cell temperatures were explored for the triple- pass configuration. The results are shown in Fig. 6 with the pumping power optimized and probe power kept at 3 mW. Increasing the temperature further to 111.5 °C and 115 °C decreased the SNR in the current setup.

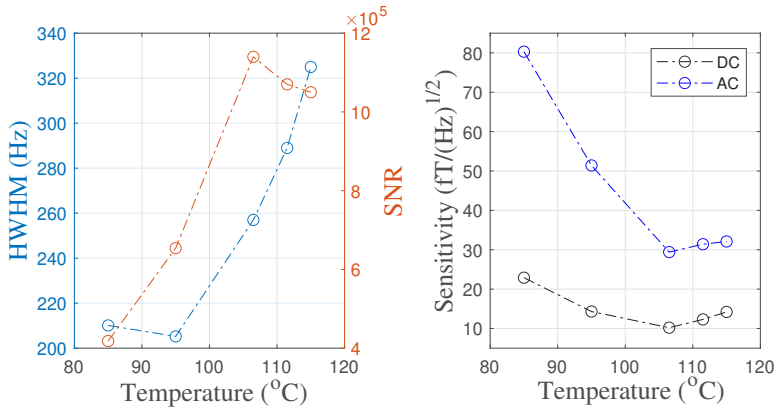

Fig. 6. Linewidth and SNR (left), and sensitivities (right) for the triple-pass probe configuration as a function of the temperature. The left panel contains the measured quantities needed to calculate the sensitivities, and the right panel containes the derived sensitivities.

An additional improvement in sensitivity for the triple- pass configuration was obtained by increasing the pump and probe beams size, as shown in row 7 in Table 2. A four-pass probe configuration was also considered and characterized. However, it was found that use of the four-pass probe led to a degradation of sensitivity, as shown in row 8 of Table 2. This due to limitations in the maximum available power, so that after three passes there is not enough probe power available for an efficient additional pass.

6. Characterization of the triple probe pass configuration

Overall, the best performances in terms of sensitivity remained the ones for a triple-pass probe configuration. The conditions for the optimal configuration are specified in row 7 in Table 2, with the pumping beam and the probe beam expanded to a diameter of 13 mm and 12.5 mm, respectively. Noise spectra measurements were performed at the frequency of 418 kHz, 107 °C, 3 mW probe power and 20 dB signal attenuation after adjusting the gradient compensation coils, with results shown in Fig. 7. From our measurements we derived a DC sensitivity improved to 8.3 fT/Hz$^{1/2}$, and an AC sensitivity of 26 fT/Hz$^{1/2}$.

The above performances in terms of sensitivity correspond to a three-fold improvement with respect to the initial configuration of single-pump and single-probe RF-AM without in-situ compensation. The demonstrated configuration is of interest for long-range detection of low-frequency fields, with potential application in underwater/underground surveillance and underwater communication. Further improvements are expected by using a larger number of fluxgate sensors, so to improve the in-situ compensation, and by increasing the available probe power, so to allow the implementation of a larger number of probe passes.

Optics EXPRESS

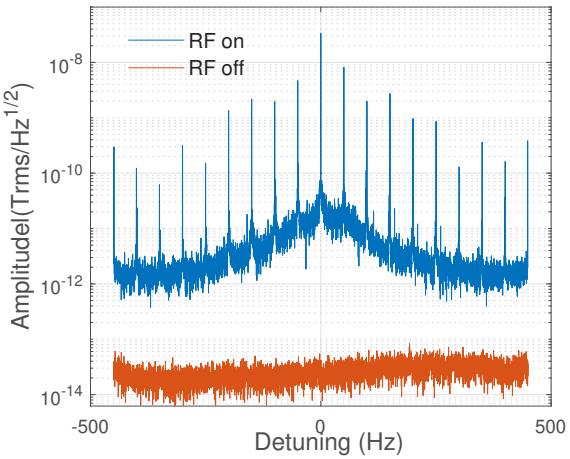

Fig. 7. Signal and noise spectrum of the triple-pass probe configuration measured with a pumping beam diameter of 13 mm, a probe beam diameter of 12.5 mm, a cell temperature of 107 °C and probe power of 3 mW. The signal spectrum was measured with RF field turned on while the noise spectrum was measured with the RF field off.

7. Conclusions

In conclusion, this work presented an experimental approach to improve the performances of an unshielded single-cell radio-frequency atomic magnetometer operating in a magnetically noisy environment. We demonstrated and quantified improvement in the sensitivity of the magnetometer by sequentially introducing the following modifications in the set-up: in-situ active cancellation of low-frequency magnetic noise, counter-propagating pumping, double- and triple-pass probe. The best performance was recorded for the configuration with counter-propagating pumping, a triple- pass probe and in-situ active compensation of the low-frequency magnetic field. For this configuration, a detailed optimization of the experimental parameters was performed, which led to an improvement in sensitivity of over a factor of three with respect to our previous single-cell single-pump magnetometer at a similar frequency, without in-situ cancellation of low-frequency magnetic noise [25].

The present work is of interest for those applications, such as the high-sensitivity detection of long-range oscillating magnetic field, where shielding or the use of gradiometers do not constitute viable options. Pathways to further improvements in performances of the RF-AM were identified.

Funding. Engineering and Physical Sciences Research Council (EP/R511638/1).

Disclosures. The authors declare no conflicts of interest.

Data availability. Data underlying the results presented in this paper are not publicly available at this time but may be obtained from the authors upon reasonable request.

References

1. D. Budker and M. Romalis, "Optical magnetometry," Nat. Phys. **3**(4), 227–234 (2007).
2. I. Kominis, T. Kornack, J. Allred, and M. V. Romalis, "A subfemtotesla multichannel atomic magnetometer," Nature **422**(6932), 596–599 (2003).
3. H. Dang, A. C. Maloof, and M. V. Romalis, "Ultrahigh sensitivity magnetic field and magnetization measurements with an atomic magnetometer," Appl. Phys. Lett. **97**(15), 151110 (2010).
4. G. Bison, R. Wynands, and A. Weis, "Dynamical mapping of the human cardiomagnetic field with a room-temperature, laser-optical sensor," Opt. Express **11**(8), 904–909 (2003).
5. Y. Yang, M. Xu, A. Liang, Y. Yin, X. Ma, Y. Gao, and X. Ning, "A new wearable multichannel magnetocardiogram system with a SERF atomic magnetometer array," Sci. Rep. **11**(1), 1–11 (2021).

Optics EXPRESS

6. E. Boto, S. S. Meyer, V. Shah, O. Alem, S. Knappe, P. Kruger, T. M. Fromhold, M. Lim, P. M. Glover, and P. G. Morris, "A new generation of magnetoencephalography: Room temperature measurements using optically-pumped magnetometers," NeuroImage **149**, 404–414 (2017).
7. M. Ledbetter, I. Savukov, D. Budker, V. Shah, S. Knappe, J. Kitching, D. Michalak, S. Xu, and A. Pines, "Zero-field remote detection of NMR with a microfabricated atomic magnetometer," Proc. Natl. Acad. Sci. **105**(7), 2286–2290 (2008).
8. S.-K. Lee, K. Sauer, S. Seltzer, O. Alem, and M. Romalis, "Subfemtotesla radio-frequency atomic magnetometer for detection of nuclear quadrupole resonance," Appl. Phys. Lett. **89**(21), 214106 (2006).
9. C. Johnson, P. D. Schwindt, and M. Weisend, "Magnetoencephalography with a two-color pump-probe, fiber-coupled atomic magnetometer," Appl. Phys. Lett. **97**(24), 243703 (2010).
10. R. Wyllie, M. Kauer, R. T. Wakai, and T. G. Walker, "Optical magnetometer array for fetal magnetocardiography," Opt. Lett. **37**(12), 2247–2249 (2012).
11. K. Kamada, Y. Ito, S. Ichihara, N. Mizutani, and T. Kobayashi, "Noise reduction and signal-to-noise ratio improvement of atomic magnetometers with optical gradiometer configurations," Opt. Express **23**(5), 6976–6987 (2015).
12. A. P. Colombo, T. R. Carter, A. Borna, Y.-Y. Jau, C. N. Johnson, A. L. Dagel, and P. D. Schwindt, "Four-channel optically pumped atomic magnetometer for magnetoencephalography," Opt. Express **24**(14), 15403–15416 (2016).
13. D. Sheng, A. R. Perry, S. P. Krzyzewski, S. Geller, J. Kitching, and S. Knappe, "A microfabricated optically-pumped magnetic gradiometer," Appl. Phys. Lett. **110**(3), 031106 (2017).
14. Y. Li, M. Ding, X. Liu, H. Cai, J. Zhao, and J. Fang, "Suppression method of AC-stark shift in SERF atomic magnetometer," IEEE Photonics J. **10**(5), 1–7 (2018).
15. A. Perry, M. Bulatowicz, M. Larsen, T. Walker, and R. Wyllie, "All-optical intrinsic atomic gradiometer with sub-20 fT/cm/$\sqrt{Hz}$ sensitivity in a 22 μT earth-scale magnetic field," Opt. Express **28**(24), 36696–36705 (2020).
16. M. Limes, E. Foley, T. Kornack, S. Caliga, S. McBride, A. Braun, W. Lee, V. Lucivero, and M. Romalis, "Portable magnetometry for detection of biomagnetism in ambient environments," Phys. Rev. Appl. **14**(1), 011002 (2020).
17. R. Zhang, R. Mhaskar, K. Smith, and M. Prouty, "Portable intrinsic gradiometer for ultra-sensitive detection of magnetic gradient in unshielded environment," Appl. Phys. Lett. **116**(14), 143501 (2020).
18. I. M. Savukov, S. Seltzer, M. Romalis, and K. Sauer, "Tunable atomic magnetometer for detection of radio-frequency magnetic fields," Phys. Rev. Lett. **95**(6), 063004 (2005).
19. C. Deans, L. Marmugi, and F. Renzoni, "Active underwater detection with an array of atomic magnetometers," Appl. Opt. **57**(10), 2346–2351 (2018).
20. C. Deans, L. Marmugi, S. Hussain, and F. Renzoni, "Electromagnetic induction imaging with a radio-frequency atomic magnetometer," Appl. Phys. Lett. **108**(10), 103503 (2016).
21. A. Wickenbrock, N. Leefer, J. W. Blanchard, and D. Budker, "Eddy current imaging with an atomic radio-frequency magnetometer," Appl. Phys. Lett. **108**(18), 183507 (2016).
22. C. Deans, L. Marmugi, and F. Renzoni, "Sub-picotesla widely tunable atomic magnetometer operating at room-temperature in unshielded environments," Rev. Sci. Instrum. **89**(8), 083111 (2018).
23. J. Ringot, P. Szriftgiser, and J. C. Garreau, "Subrecoil Raman spectroscopy of cold cesium atoms," Phys. Rev. A **65**(1), 013403 (2001).
24. G. O. Forte, G. Farrher, L. R. Canali, and E. Anoardo, "Automatic shielding-shimming magnetic field compensator for excluded volume applications," IEEE Trans. Contr. Syst. Technol. **18**(4), 976–983 (2010).
25. H. Yao, B. Maddox, Y. Cohen, and F. Renzoni, "Optimisation of a radio-frequency atomic magnetometer: a Uniform Design approach," Opt. Express **30**(3), 3566–3576 (2022).
26. J. Yuchen, L. Zhanchao, Z. Binquan, L. Xiaoyang, W. Wenfeng, P. Jinpeng, D. Ming, Z. Yueyang, and F. Jiancheng, "Pump beam influence on spin polarization homogeneity in the nuclear magnetic resonance gyroscope," J. Phys. D: Appl. Phys. **52**(35), 355001 (2019).
27. H. Yao, H. Zhang, D. Ma, J. Zhao, and M. Ding, "In situ determination of alkali metal density using phase-frequency analysis on atomic magnetometers," Meas. Sci. Technol. **29**(9), 095005 (2018).
28. M. Auzinsh, D. Budker, and S. Rochester, *Optically polarized atoms: understanding light-atom interactions* (Oxford University Press, 2010).
29. M. Romalis, "Hybrid optical pumping of optically dense alkali-metal vapor without quenching gas," Phys. Rev. Lett. **105**(24), 243001 (2010).
30. I. Sulai, R. Wyllie, M. Kauer, G. Smetana, R. Wakai, and T. Walker, "Diffusive suppression of AC-stark shifts in atomic magnetometers," Opt. Lett. **38**(6), 974–976 (2013).
31. E. Babcock, I. Nelson, S. Kadlecek, B. Driehuys, L. Anderson, F. W. Hersman, and T. G. Walker, "Hybrid spin-exchange optical pumping of ^{3}He," Phys. Rev. Lett. **91**(12), 123003 (2003).
32. C. Alcock, V. Itkin, and M. Horrigan, "Vapour pressure equations for the metallic elements: 298–2500K," Can. Metall. Q. **23**(3), 309–313 (1984).
33. J. Zhao, G. Liu, J. Lu, M. Ding, Y. Ma, J. Ji, K. Yang, D. Ma, B. Xing, and N. Zhang, "Improvement of spin polarization spatial uniformity in optically pumped atomic magnetometers based on counter-propagating pump beams and atomic diffusion," Meas. Sci. Technol. **32**(3), 035902 (2021).
34. S. Li, P. Vachaspati, D. Sheng, N. Dural, and M. V. Romalis, "Optical rotation in excess of 100 rad generated by Rb vapor in a multipass cell," Phys. Rev. A **84**(6), 061403 (2011).